Research Square

Preprints are preliminary reports that have not undergone peer review.
They should not be considered conclusive, used to inform clinical practice,
or referenced by the media as validated information.

Field-angle evolution from spin flipping to continuous reorientation in layered CrSBr

Jisung Lee
Korea Basic Science Institute
Suwan Kim
Chungnam National University
Junseop Kim
Chungnam National University
Dooyong Lee
Kyungpook National University
Zdenek Sofer
University of Chemistry and Technology Prague
Kyongmo An
Chungbuk National University
Chang-woo Cho
chang-woo.cho@cnu.ac.kr

Chungnam National University

Article

Keywords:

Posted Date: November 17th, 2026

DOI: https://doi.org/10.21203/rs.3.rs-11546073/v1

License: This work is licensed under a Creative Commons Attribution 4.0 International License.
Read Full License

Additional Declarations: No competing interests reported.

Abstract

CrSBr is a layered magnetic semiconductor in which antiferromagnetically coupled ferromagnetic layers respond differently to magnetic fields applied along the crystallographic axes. Here, we investigate spin reorientation in bulk CrSBr through field- and angle-dependent magnetization measurements over a range of temperatures, complemented by angular magnetoresistance measurements. As the field rotates from the easy *b*-axis toward the *a*-axis, the magnetization evolves from an abrupt spin-fliping to continuous canting. At intermediate angles, a sharp susceptibility feature accompanies a broader contribution, and the reorientation extends over a wider field interval. A two-sublattice model with independently determined exchange coupling and *g*-factors captures the main angular trends using a fixed in-plane anisotropy $K_{ab} \approx 0.18$ K. The magnetoresistance crossover occurs at lower fields than the upper characteristic magnetic field H_{up}, without a direct assignment to a particular spin configuration. These results connect abrupt reversal and continuous canting within a common description.

Introduction

Layered van der Waals magnets allow magnetic order to be studied from bulk crystals down to individual atomic layers and incorporated into heterostructures with various two-dimensional materials [1, 2]. Their appeal lies not only in reducing the thickness of a magnet, but also in controlling the relative alignment of neighboring magnetic layers. In systems with weak interlayer magnetic coupling, an applied field can change this alignment and thereby modify charge transport easily, as demonstrated by spin-filter tunneling devices [3]. Understanding how layer magnetizations evolve under a field is therefore important both for the physics of low-dimensional magnetism and for interpreting spin-dependent transport.

Among these materials, CrSBr combines air stability, semiconducting transport, and strongly anisotropic magnetism [4, 5]. Its ferromagnetic layers order antiferromagnetically below $T_{\mathrm{N}} \approx 132$ K, with the *b*-axis as the easy axis, the *a*-axis as the intermediate axis, and the *c*-axis as the hard axis [6–8]. Magnetic alignment affects both interlayer electronic hybridization and electrical conduction, making CrSBr particularly useful for studying the connection between spin configuration and electronic behavior [4, 9, 10]. In addition, air stability facilitates experiments on both bulk crystals and exfoliated devices without encapsulation, although the ordering temperature remains below room temperature [5].

Research on CrSBr has progressed from identifying its magnetic order to determining microscopic interactions and controlling its electronic properties. Neutron scattering and magnetic resonance have constrained the exchange interactions and magnetic anisotropy [8, 11–13], while magneto-optical and transport studies have demonstrated the sensitivity of electronic states and conduction to magnetic alignment [4, 9, 10, 14]. Spatial imaging has resolved domain nucleation and field-induced magnetic transitions [15, 16]. More recent work has shown that pressure, strain, and interfacial charge transfer can modify interlayer coupling or anisotropy and alter field-driven spin reorientation [17–19]. These results

make a quantitative description of spin reorientation relevant to both single crystals and engineered heterostructures.

Despite this progress, identifying a transition field does not fully characterize how magnetization evolves throughout a field sweep. Angle-dependent electron spin resonance (ESR) and magnetotransport measurements have demonstrated sensitivity to field orientation [8, 12, 20], but they probe excitation energies or electrical conduction rather than directly tracing the static magnetization. Additional information is needed because different sets of magnetic parameters can produce identical phenomena such as a sharp easy-axis anomaly. In the two-sublattice description, the magnetic behavior is governed by the balance between interlayer exchange $J_\perp$ and in-plane anisotropy $K_{ab} = D - E$, where D and E are the biaxial single-ion anisotropy parameters [8]. An easy-axis spin-flop phase is allowed for $0 < K_{ab} < 2J_\perp$, whereas $K_{ab} > 2J_\perp$ gives a direct spin flip [8, 11, 17]. Previous ESR and imaging studies have reported behavior in both regimes [8, 11, 15], raising questions about the possible influence of growth conditions and other sample-dependent factors. This variation motivates comparing resonance and static magnetization measurements on crystals from the same growth batch. Here, we use crystals from the batch examined in the earlier ESR study [8] to determine whether the independently obtained magnetic parameters also account for the magnetization across field strengths and in-plane angles.

For this purpose, we measure magnetization over field sweeps at various angles within the *ab* plane of bulk CrSBr and follow its evolution with temperature. We compare the measured curves with a two-sublattice model using exchange coupling and g-factors determined by ESR [8]. The intermediate-angle curves and the *a*-axis saturation scale jointly favor K_{ab} near 0.18 K, close to the ESR value $D - E = 0.1882$ K, without readjusting the parameters at each angle. First and second field derivatives of the magnetization characterize the widening reorientation interval. Angular magnetoresistance measurements provide a separate field-angle comparison of the transport feature with the magnetic characteristic fields.

Results

Crystal structure and magnetic properties of CrSBr

Figure 1a shows the orthorhombic structure of CrSBr and its A-type antiferromagnetic order [4, 6, 13, 21, 22]. The magnetizations $\mathbf{m_1}$ and $\mathbf{m_2}$ of alternating layers point along opposite easy-axis directions, ±*b*, at zero field [6, 8, 13]. The field angle ϕ is measured from the *b*-axis within the *ab* plane, with $\phi = 0°$ for $H \| b$ and $\phi = 90°$ for $H \| a$. Rotating the field between these directions allows us to follow the change from easy-axis reversal to transverse canting in the crystal.

The temperature dependences of conductance $G(T)$ and magnetization $M(T)$, shown in Fig. 1b**&c**, identify the magnetically ordered regime. In Fig. 1b, $G(T)$ has a semiconducting temperature dependence, with a pronounced feature in dG/dT near $T_N \approx 132$ K [4, 6, 10]. The $M(T)$ curves along the *a*- and *b*-axes become strongly anisotropic across the same temperature range, as presented in Fig. 1c. These measurements

confirm that conductance is sensitive to magnetic ordering and identify the two in-plane directions used below.

Temperature- and angle-dependent magnetization in the ab-plane

Figure 2 follows $M(H)$ as the field rotates within the *ab* plane at selected temperatures of 5 K, 50 K, and 90 K. The complete temperature series appears in **Supplementary Fig. S1**. At 5 K and $\phi = 0°$ (Fig. 2a), the normalized magnetization (M/M_s) exhibits a pronounced step-like behavior with weak hysteresis, consistent with the previously reported easy-axis spin flip [6, 8]. As ϕ increases, a gradual field-dependent contribution develops around the step and extends over a wider range. The sharp component remains visible at intermediate angles around 60° but weakens toward $H \| a$, where magnetization approaches saturation continuously. Increasing temperature broadens this feature and reduces the characteristic fields while preserving this general angular progression.

In Fig. 2d–f, we plot $\mathrm{d}(M/M_s)/\mathrm{d}H$, proportional to the differential susceptibility, which reveals how the magnetization change is distributed over the field sweep. Near $H \| b$ ($\phi = 0°$, 15°), $\mathrm{d}(M/M_s)/\mathrm{d}H$ is concentrated in a narrow peak. At intermediate angles ($\phi = 30°$, 45°, 60°), this peak is accompanied by a broader contribution. Near $H \| a$ ($\phi = 75°$, 90°), the magnetization change extends over a larger field range. Field rotation thus changes both the shape and the extent of the anomaly. To compare these evolving curves consistently, we track the low- and high-field flanks of the main susceptibility feature.

Figure 2g–i show $\mathrm{d}^2(M/M_s)/\mathrm{d}H^2$, from which H_{low} and H_{up} are identified as the outer curvature extrema on the two flanks of the main susceptibility anomaly (dashed lines and vertical arrows). For $H \| b$, the markers delimit the finite experimental width of the step-like behavior. Their separation grows toward $H \| a$, mainly through the increase in H_{up}. Figure 2j–l summarize the temperature dependences at $\phi = 0°$, 45°, and 90°. H_{low} varies comparatively weakly, whereas H_{up} decreases more strongly on approaching T_{N}, particularly near $H \| a$. It should be mentioned that these curvature fields characterize the measured magnetization curves rather than define independent thermodynamic phase boundaries. The finite peak widths and limited angular resolution make it difficult to determine exactly where the sharp feature disappears.

Reduced two-layer-sublattice model

To describe spin flipping and canting more precisely, we use a reduced equilibrium model of the A-type magnetic structure. Inelastic neutron scattering finds strong ferromagnetic exchange within the layers and much weaker interlayer coupling [13], motivating a uniform spin direction for each alternating layer sublattice. The unit vectors $\mathbf{n_1}$ and $\mathbf{n_2}$ are confined to the *ab* plane and written as $\mathbf{n_i} = \sin\theta_i\,\hat{\mathbf{a}} + \cos\theta_i\,\hat{\mathbf{b}}$, with θ_i measured from the *b*-axis (see Fig. 1a). Their magnitudes remain fixed while their equilibrium directions vary with field. The model does not prescribe a spin flip or a gradual rotation in advance. The magnetization curve follows from energy minimization.

For a magnetic field $\mathbf{H} = H(\sin\phi\,\hat{\mathbf{a}} + \cos\phi\,\hat{\mathbf{b}})$, the in-plane reduction of the microscopic Hamiltonian gives $K_{ab} = D - E$ after removing an orientation-independent constant [8]. Using exchange and anisotropy coefficients expressed in Kelvin, the reduced energy is

$E(\theta_1, \theta_2)/k_B = 4J_\perp S^2 \cos(\theta_1 - \theta_2) - K_{ab} S^2(\cos^2\theta_1 + \cos^2\theta_2) - (\mu_B/k_B) S H(g_b \cos\phi(\cos\theta_1 + \cos\theta_2) + g_a \sin\phi(\sin\theta_1 + \sin\theta_2))$.

Here, $S = 3/2$ for Cr^{3+}, and g_a and g_b are the in-plane g-factors. For each (H, ϕ), minimization with respect to θ_1 and θ_2 gives the equilibrium directions and the field-projected moment. We use the resonance-derived $J_\perp$, g_a, and g_b [8] and compare several values of K_{ab} in the following. The Calculation subsection of Methods provides further details on the energy reduction, moment normalization, numerical procedure, and easy-axis criterion $K_{ab} = 2J_\perp$.

Spin flipping and canting within a common magnetic model

Figure 3a compares the M/M_s calculation for $K_{ab} = 0.18$ K with the 5 K measurements at $\phi = 0°$, 45°, and 90° (red dashed lines). The other parameters are $J_\perp = 0.069$ K, $S = 3/2$, $g_a = 2.05$, and $g_b = 1.88$ [8]. This single set describes the easy-axis step and the gradual approach to saturation along the a-axis. The 45° curve supplies a more demanding comparison, where the simulation curve follows both the gradual central variation in magnetization and its field extent, although the measured transitions are rounded rather than ideal steps. The susceptibility makes these differences, and their dependence on K_{ab}, easier to distinguish.

Figure 3b exhibits the susceptibility at $\phi = 0°$ for $K_{ab} = 0.04$ K, 0.10 K, 0.18 K, 0.24 K, and 0.30 K. The first two values lie below $2J_\perp = 0.138$ K and permit an easy-axis spin flop, whereas the other three give a direct spin flip. Within the direct spin-flip regime, the ideal easy-axis switching field is independent of K_{ab}. Additionally, a narrow easy-axis peak can occur in either regime, so its presence alone does not discriminate between them. At 45° (Fig. 3c), the lower-anisotropy cases ($K_{ab} = 0.04$ K, 0.10 K) have a smoother susceptibility profile spread over a wider field interval, while the higher-anisotropy cases ($K_{ab} =$ 0.18 K, 0.24 K, 0.30 K) retain a localized feature. The measured peak and broad contribution favor the latter. This comparison does not, however, distinguish 0.18 K uniquely from 0.24 or 0.30 K, nor does a peak on a broad background imply two coexisting phases.

The a-axis magnetization ($\phi = 90°$) provides a further constraint as presented in Fig. 3d. As described in **Supplementary Section 4**, its saturation field satisfies $(g_a\mu_B/k_B)H_{sat} = 2S(4J_\perp + K_{ab})$, increasing with K_{ab} at fixed exchange. Values of 0.18 K, 0.24 K, and 0.30 K give $H_{sat} \approx 0.99$ T, 1.12 T, and 1.25 T, respectively. The measured approach to saturation is closest to the prediction for 0.18 K, whereas the calculations for 0.04 K and 0.10 K reach saturation below the observed field range. Therefore, the $\phi = 45°$ line shape and

the *a*-axis field scale favor K_{ab} near 0.18 K among the values considered. This value is also consistent with the ESR-derived $D - E$ = 0.1882 K [8].

Field and angle dependence of magnetic reorientation and transport

Figure 4 combines the full calculated susceptibility map for K_{ab} = 0.18 K with experimentally obtained H_{low} and H_{up} at 5 K. The same parameter set used in Fig. 3 describes the overall angular widening. H_{low} and H_{up} are closely spaced near the *b*-axis and separate toward the *a*-axis, primarily through the increase in H_{up}. The calculated map contains a sharp feature over part of the angular range (up to ~ 60°) and an extended contribution from continuous rotation. Both arise from the equilibrium solutions of the same energy expression as field and angle are varied. This map supports a comparison of the complete reorientation process without assigning separate crossover boundaries at specific angles. Furthermore, the magnetoresistance crossover angles ϕ_c, shown as purple triangles at their corresponding fields, are overlaid on the map. Notably, these crossover points place at lower fields than H_{up} and appear to follow a qualitatively similar angular trend.

Discussion

The agreement with the angular magnetization indicates that the resonance-derived parameters also provide a useful description of static spin reorientation in CrSBr. A single parameter set connects abrupt reversal and continuous canting without separate adjustments at each angle. This consistency supports the applicability of the microscopic Hamiltonian beyond the excitation spectrum from which its parameters were obtained. The inferred K_{ab} near 0.18 K should nevertheless be understood as the value favored among the discrete choices considered here, rather than a statistical determination of the anisotropy.

The magnetoresistance crossover points ϕ_c follow a similar angular trend to H_{up} but locate at lower fields. This difference may reflect the distinct sensitivities of magnetization and transport to the magnetic state. Magnetization measures the net moment projected along the field, whereas resistance can depend on the relative alignment of neighboring layers through spin-dependent electronic coupling [9, 10]. Hopping transport provides one possible mechanism for this sensitivity. In vertical CrSBr devices, magnetic alignment has been linked to changes in the conduction-band edge and accessible interlayer hopping paths [14]. Because hopping resistance depends exponentially on the relevant energy barriers and hopping distances, changes in these quantities can produce a substantial change in resistance without a comparably sharp feature in magnetization. Such sensitivity could contribute to the separation between the ϕ_c and H_{up} in the field-angle map.

The two-sublattice model describes each ferromagnetic layer by a uniform magnetization and does not include domain formation, domain-wall motion, or spatial variations in magnetic parameters. Spatially resolved measurements have demonstrated domain nucleation and propagation in CrSBr [15, 16]. Such

processes may contribute to the rounded experimental anomalies, but their role in the present crystals is not determined by these measurements. The small kinks in the nominal $H\|a$ curves are also not reproduced by the ideal model, which predicts a linear increase in magnetization below saturation along this direction. The model thus captures the main angular trends and characteristic field scales, while the origins of the rounding and small kinks remain to be clarified.

Conclusion

In summary, angle-dependent magnetization reveals how easy-axis spin flipping evolves into continuous canting as the field rotates within the *ab* plane of bulk CrSBr. Intermediate-angle measurements resolve sharp and gradual contributions to the magnetization change over a widening field interval. A two-sublattice model with resonance-derived exchange and *g*-factors captures this evolution using a fixed K_{ab} near 0.18 K, consistent with the earlier ESR result. The magnetoresistance crossover follows a similar angular trend to H_{up} but occurs at lower fields, indicating distinct characteristic scales for transport and magnetization. By combining intermediate-angle line shapes with the transverse saturation field, our measurements distinguish magnetic parameter sets that produce the same easy-axis transition and support a common description of abrupt reversal and continuous canting in CrSBr.

Methods

Magnetization and magnetotransport measurements

Bulk CrSBr single crystals from the same growth batch as those investigated in the earlier ESR study were used [8]. Magnetization was measured using a Quantum Design MPMS 5 T system at Korea Basic Science Institute (KBSI). Isothermal $M(H)$ curves were recorded between − 1.5 T and 1.5 T with the field oriented within the *ab* plane in 15° increments, where $\phi = 0°$ and 90° denote $H\|b$ and $H\|a$, respectively. The full temperature series is shown in **Supplementary Fig. S1**. Except for data measured at 150 K, $M(H)$ was normalized by the saturation magnetization. At 150 K, the curves were normalized to their measured value at 1.5 T because 150 K is higher than T_N. Temperature-dependent magnetization along both *a*- and *b*-axes was measured under zero-field-cooled (ZFC) and field-cooled (FC) (Fig. 1c).

Because CrSBr exhibits semiconducting behavior [4, 10], the current was measured using lock-in detection in a two-probe current-measurement configuration. An AC bias voltage between 0.01 and 0.1 *V* was applied at a frequency of 10–20 Hz. The in-phase current was recorded, and conductance (resistance) was calculated as $G = I/V$ ($R = 1/G$). Angular magnetoresistance was measured by sweeping the in-plane field angle at fixed fields selected between 0.1 T and 1.1 T. **Supplementary Fig. S2** shows selected-field traces at 10 K, 50 K, 90 K, and 130 K. The two-probe configuration includes contact contributions, so the transport data are used to compare the electrical feature with magnetic reorientation rather than to determine an intrinsic resistivity.

Calculation

We use the two-sublattice Hamiltonian of the earlier ESR analysis [8], which gave $J_\perp$ = 0.0694 K, D = 0.3956 K, and E = 0.2074 K. We retain the exchange convention of that analysis, in which the two-sublattice exchange term is $4J_\perp(S_1 \cdot S_2)$. Throughout the field-dependent expressions, H denotes the applied-field quantity expressed in tesla ($\mu_0 H$ in SI notation). With exchange and anisotropy coefficients expressed in Kelvin, the exchange, single-ion, and in-plane Zeeman terms are

$$\mathcal{H}/k_B = 4J_\perp S_1 \cdot S_2 + \Sigma_{i=1,2}[-D(S_i^b)^2 + E\{(S_i^c)^2 - (S_i^a)^2\}] - (\mu_B/k_B)\Sigma_{i=1,2}(g_a H_a S_i^a + g_b H_b S_i^b).$$

Each Cr^{3+} moment is written as $S_i = S\, n_i$ with S = 3/2 and $\mathbf{n_i} = \sin\theta_i\, \hat{\mathbf{a}} + \cos\theta_i\, \hat{\mathfrak{b}}$. The field components are $H_a = H \sin\phi$ and $H_b = H \cos\phi$. The exchange contribution becomes $S_1 \cdot S_2 = S^2 \cos(\theta_1 - \theta_2)$.

For spins confined to the ab plane, $S_i^c = 0$, $S_i^a = S \sin\theta_i$, and $S_i^b = S \cos\theta_i$. The single-ion term for each sublattice reduces to $-DS^2\cos^2\theta_i - ES^2\sin^2\theta_i = -(D - E)S^2\cos^2\theta_i - ES^2$. The last term is independent of spin direction and is omitted, giving $K_{ab} = D - E$.

The resulting in-plane energy is

$$E/k_B = 4\, J_\perp\, S^2 \cos(\theta_1 - \theta_2) - K_{ab}\, S^2(\cos^2\theta_1 + \cos^2\theta_2) - (\mu_B/k_B)\, S\, H(g_b \cos\phi(\cos\theta_1 + \cos\theta_2) + g_a \sin\phi(\sin\theta_1 + \sin\theta_2)).$$

For each (H, ϕ) pair, a coarse search over θ_1 and θ_2 was followed by local refinement to identify the global minimum. The field-projected magnetic moment was calculated from $-\partial E/\partial H$ as

$$M_{\parallel} = \mu_B\, S(g_b \cos\phi(\cos\theta_1 + \cos\theta_2) + g_a \sin\phi(\sin\theta_1 + \sin\theta_2)).$$

The field-projected moment was normalized by the calculated saturation value for each field direction before numerical differentiation. We use $J_\perp$ = 0.069 K, S = 3/2, g_a = 2.05, g_b = 1.88, and μ_B/k_B = 0.6717 K/T. The exchange and g-factors are obtained from the resonance values [8]. The main comparison uses K_{ab} = 0.18 K, and the parameter series contains the five values listed in Fig. 3. No angle-dependent adjustment of these parameters is made.

For $H \| b$, the canted branch gives $(g_b\mu_B/k_B)H_{sf} = 2S[K_{ab}(4J_\perp - K_{ab})]^{1/2}$ and $(g_b\mu_B/k_B)H_{sat} = 2S(4J_\perp - K_{ab})$ [8]. These fields merge at $K_{ab} = 2J_\perp$. Thus $0 < K_{ab} < 2J_\perp$ allows an intermediate canted state, whereas $K_{ab} > 2J_\perp$ produces a direct first-order spin flip at $(g_b\mu_B/k_B)H_{cr} = 4J_\perp S$. Because the calculation selects the global equilibrium state, it does not reproduce hysteresis or metastable domain dynamics.

Declarations

Competing interests

The authors declare no competing interests.

Funding

This research was supported by Global-Learning & Academic research institution for Master's·PhD students, Postdocs (G-LAMP) Program of the National Research Foundation of Korea (NRF) grant funded by the Ministry of Education (No. RS-2025-25442707). This work was supported in part by the National Research Foundation of Korea (NRF) (Grant No. RS-2025-25419722) and in part by the Creation of the quantum information science R&D ecosystem (based on human resources) (RS-2023-00256050) through the NRF, funded by the Korean government (Ministry of Science and ICT, MSIT). This research was supported by the Commercialization Promotion Agency for R&D Outcomes(COMPA) funded by the Ministry of Science and ICT(MSIT) (2710107300). This research was supported by the Technology Innovation Program (or Industrial Strategic Technology Development Program-Public-private joint investment semiconductor R&D program(K-CHIPS) to foster high-quality human resources) ("RS-2023-00236642", Development of etching process and diagnostic technology using precursor with low GWP for next generation semiconductor process) funded By the Ministry of Trade, Industry & Energy(MOTIE, Korea)(1415187459).

Author Contribution

J.L., S.K., J.K., and C.-w.C. performed the magnetization and transport measurements and analyzed the data. D.L. and K.A. contributed to data interpretation. Z.S. provided the single crystals. The manuscript was prepared by C.-w.C. and all authors were involved in discussions and contributed to the manuscript.

Acknowledgement

We thank Benjamin A. Piot for helpful discussions and comments on the manuscript.

Data Availability

The data that support the findings of this study are available from the corresponding author upon reasonable request.

References

1. Huang, B. et al. Layer-dependent ferromagnetism in a van der Waals crystal down to the monolayer limit. *Nature* **546**, 270–273 (2017).
2. Gibertini, M., Koperski, M., Morpurgo, A. F. & Novoselov, K. S. Magnetic 2D materials and heterostructures. *Nat. Nanotechnol*. **14**, 408–419 (2019).

3. Song, T. et al. Giant tunneling magnetoresistance in spin-filter van der Waals heterostructures. *Science* **360**, 1214–1218 (2018).
4. Telford, E. J. et al. Layered Antiferromagnetism Induces Large Negative Magnetoresistance in the van der Waals Semiconductor CrSBr. *Adv. Mater.* **32**, 2003240 (2020).
5. Ziebel, M. E. et al. CrSBr: An Air-Stable, Two-Dimensional Magnetic Semiconductor. *Nano Lett.* **24**, 4319–4329 (2024).
6. Göser, O., Paul, W. & Kahle, H. G. Magnetic properties of CrSBr. *J. Magn. Magn. Mater.* **92**, 129–136 (1990).
7. Yang, K., Wang, G., Liu, L., Lu, D. & Wu, H. Triaxial magnetic anisotropy in the two-dimensional ferromagnetic semiconductor CrSBr. *Phys. Rev. B*. **104**, 144416 (2021).
8. Cho, C. W. et al. Microscopic parameters of the van der Waals CrSBr antiferromagnet from microwave absorption experiments. *Phys. Rev. B*. **107**, 094403 (2023).
9. Wilson, N. P. et al. Interlayer electronic coupling on demand in a 2D magnetic semiconductor. *Nat. Mater.* **20**, 1657–1662 (2021).
10. Telford, E. J. et al. Coupling between magnetic order and charge transport in a two-dimensional magnetic semiconductor. *Nat. Mater.* **21**, 754–760 (2022).
11. Cham, T. M. J. et al. Anisotropic Gigahertz Antiferromagnetic Resonances of the Easy-Axis van der Waals Antiferromagnet CrSBr. *Nano Lett.* **22**, 6716–6723 (2022).
12. Moro, F. et al. Revealing 2D magnetism in a bulk CrSBr single crystal by electron spin resonance. *Adv. Funct. Mater.* **32**, 2207044 (2022).
13. Scheie, A. et al. Spin waves and magnetic exchange Hamiltonian in CrSBr. *Adv. Sci.* **9**, 2202467 (2022).
14. Lin, X. et al. Influence of magnetism on vertical hopping transport in CrSBr. *Phys. Rev. Res.* **6**, 013185 (2024).
15. Yu, J. et al. Direct imaging of antiferromagnet–ferromagnet phase transition in van der Waals antiferromagnet CrSBr. *Adv. Funct. Mater.* **34**, 2307259 (2024).
16. Zur, Y. et al. Magnetic imaging and domain nucleation in CrSBr down to the 2D limit. *Adv. Mater.* **35**, 2307195 (2023).
17. Pawbake, A. et al. Magneto-Optical Sensing of the Pressure Driven Magnetic Ground States in Bulk CrSBr. *Nano Lett.* **23**, 9587–9593 (2023).
18. Henríquez-Guerra, E. et al. Strain engineering of magnetoresistance and magnetic anisotropy in CrSBr. *Adv. Mater.* **38**, 2506695 (2026).
19. Hong, C. et al. Charge transfer governed interlayer magnetic coupling and symmetry breaking in a van der Waals magnet. *Nat. Commun.* **16**, 9498 (2025).
20. Boix-Constant, C. et al. Multistep magnetization switching in orthogonally twisted ferromagnetic monolayers. *Nat. Mater.* **23**, 212–218 (2024).

21. López-Paz, S. A. et al. Dynamic magnetic crossover at the origin of the hidden-order in van der Waals antiferromagnet CrSBr. *Nat. Commun.* **13**, 4745 (2022).
22. Lee, K. et al. Magnetic order and symmetry in the 2D semiconductor CrSBr. *Nano Lett.* **21**, 3511–3517 (2021).

Figures

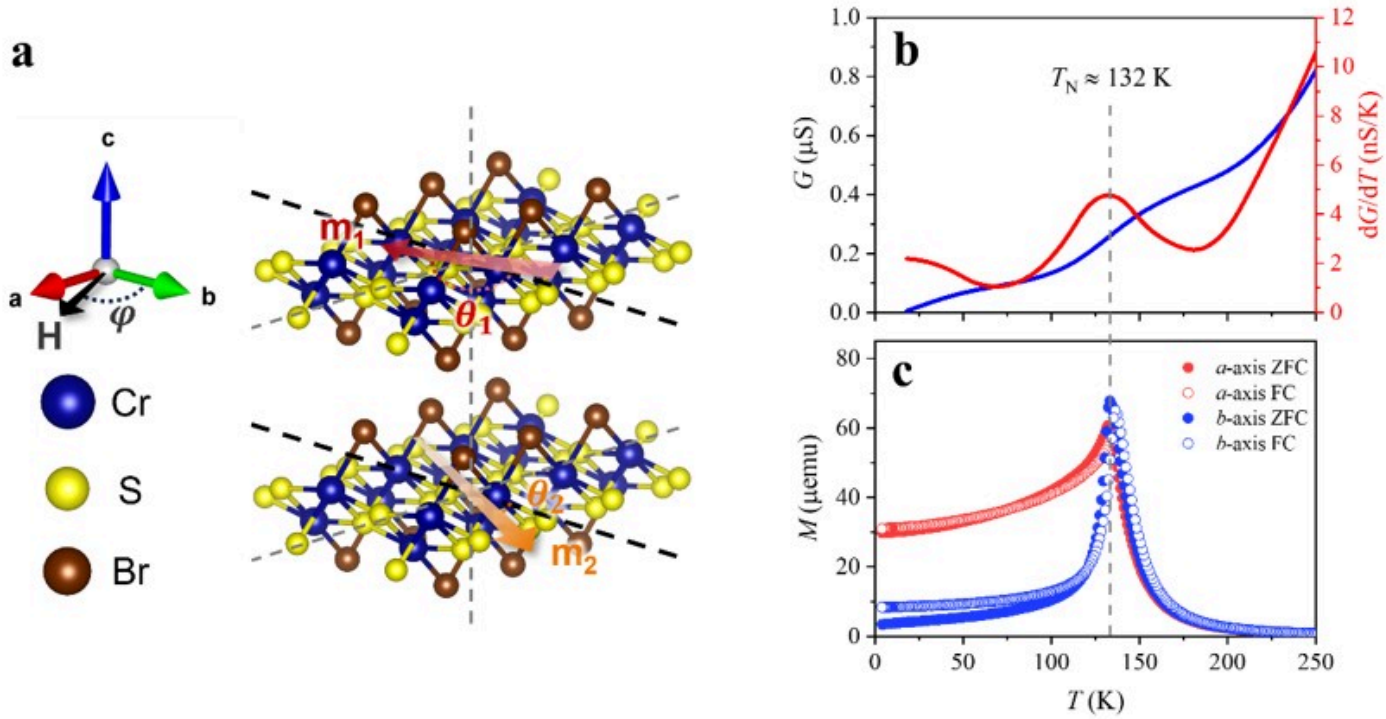


Figure 1

Crystal structure, measurement geometry, and basic characterization of CrSBr. a, Layered crystal structure, schematic layer magnetizations and the definition of the in-plane field angle ϕ. The *b*-axis is the magnetic easy axis and $\phi = 0°$ corresponds to $H \| b$. The () denote the angle between the layer magnetization $\mathbf{m_1}(\mathbf{m_2})$ and *b*-axis **b**, Temperature dependence of the conductance *G* and its derivative d*G*/d*T*. The dashed line marks $T_N \approx 132$ K. **c**, Temperature-dependent magnetization measured along the *a*- and *b*-axes under ZFC (filled symbols) and FC (open symbols) conditions.

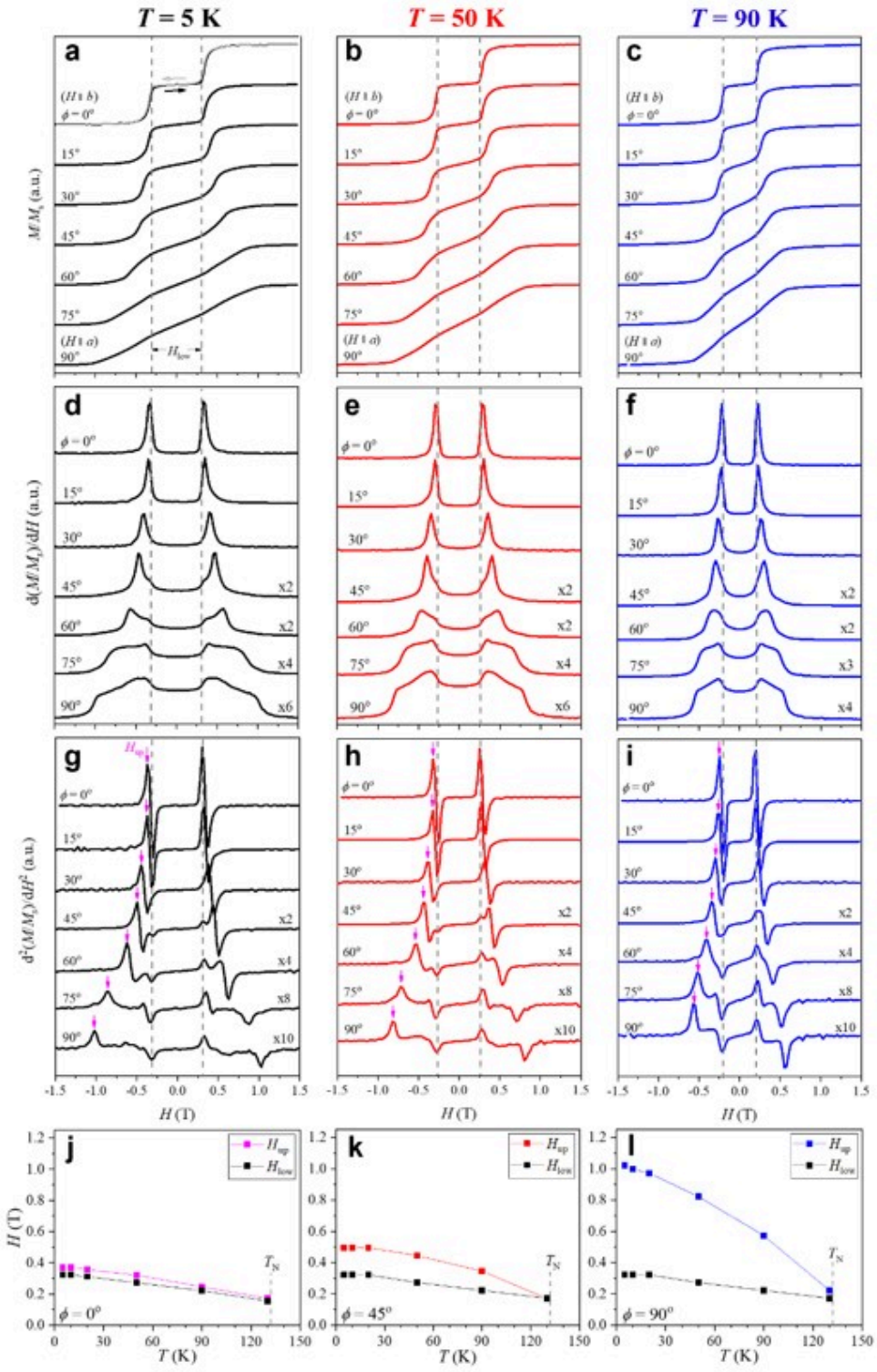


Figure 2

Angle-dependent evolution of magnetization in the *ab*-plane. a-c, Normalized $M(H)$ curves at T = 5 K, 50 K, and 90 K for field angles from $H \| b$ (ϕ = 0°) to $H \| a$ (ϕ = 90°). **d-f**, Corresponding $d(M/M_S)/dH$ curves, showing the evolution from a narrow easy-axis anomaly to a broad high-angle anomaly. **g-i**, Second

derivatives $d^2(M/M_s)/dH^2$ used to extract the lower and upper characteristic fields, H_{low} and H_{up}. **j-l**, Temperature dependence of H_{low} and H_{up} at ϕ = 0°, 45°, and 90°. The dashed vertical line marks T_N.

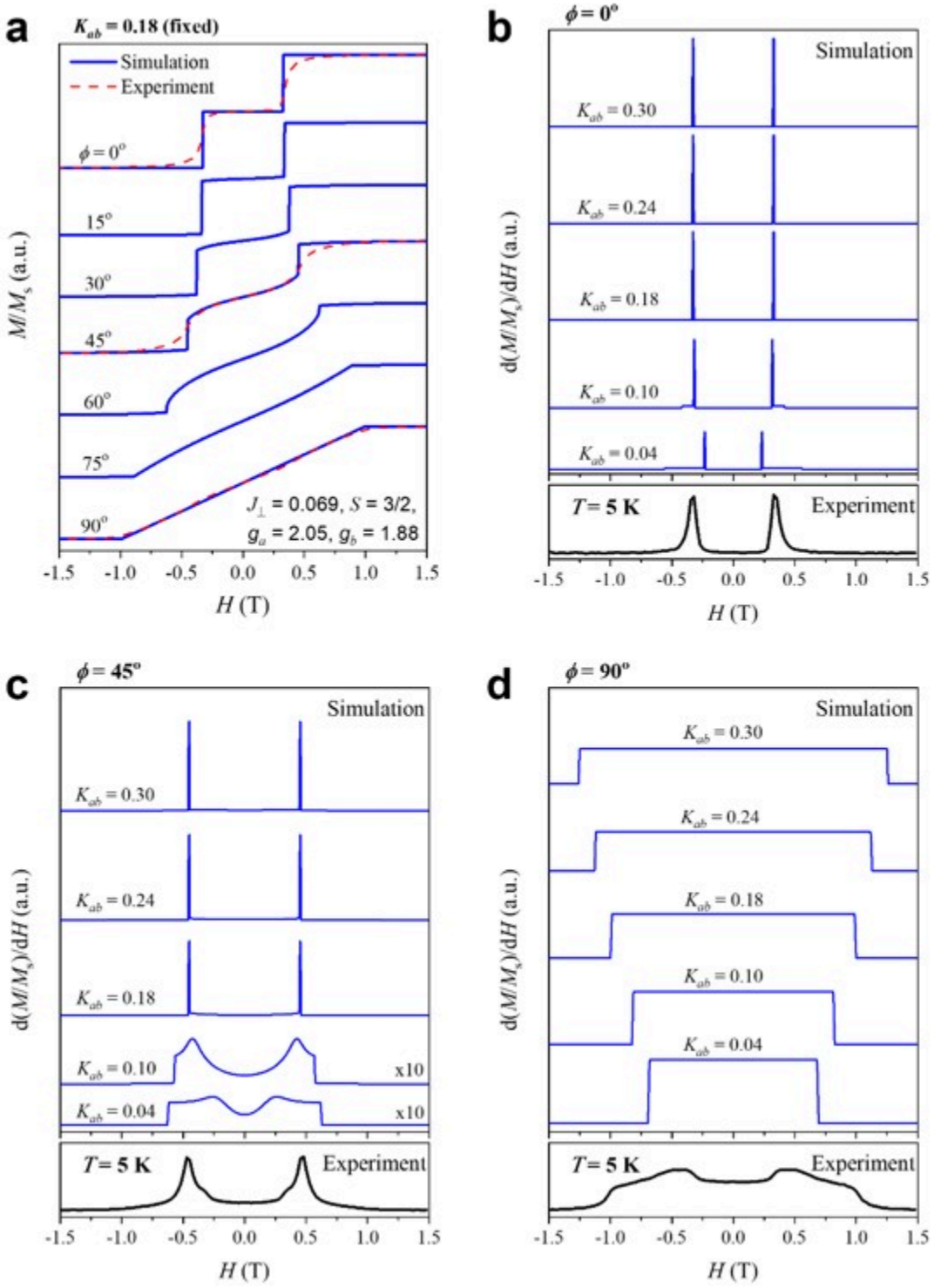


Figure 3

Spin flipping and canting in a common two-layer-sublattice model. a, Simulated $M(H)$ curves for K_{ab} = 0.18 K at selected field angles with a common parameter set, using $J_\perp$ = 0.069 K, S = 3/2, g_a = 2.05, and

g_b = 1.88. Red dashed curves show representative experimental data at ϕ = 0°, 45°, and 90°. **b–d,** Simulated d(M/M_s)/dH for K_{ab} = 0.04 K, 0.10 K, 0.18 K, 0.24 K, and 0.30 K at ϕ = 0°, 45°, and 90°, respectively. The corresponding 5 K data are shown below each panel. The low-anisotropy traces in **c** are multiplied by ten, as indicated. The comparison considers the line shape and field extent across the calculated parameter sets.

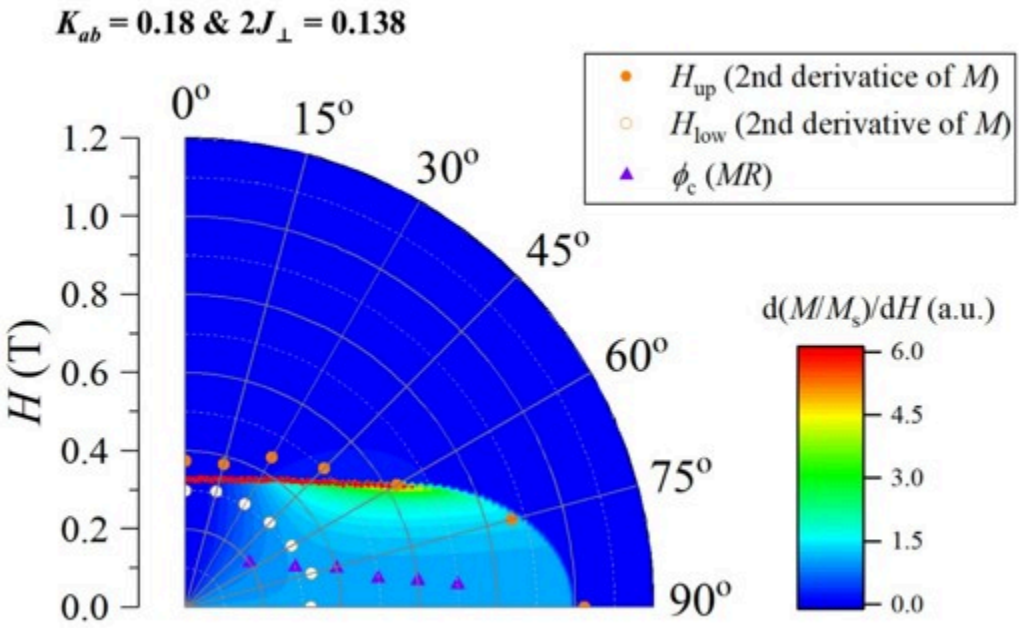


Figure 4

Calculated field-angle susceptibility and experimental characteristic fields. The polar color map shows d(M/M_s)/dH for K_{ab} = 0.18 K and $2J_\perp$ = 0.138 K. The radial coordinate is magnetic field and the azimuthal coordinate is the in-plane field angle measured from the b-axis. Filled and open orange symbols denote H_{up} and H_{low}, respectively, extracted from the second derivative of magnetization at 5 K. Purple triangles denote the magnetoresistance crossover angle ϕ_c measured at 10 K. The overlay compares the angular trends and distinct field scales of the magnetic and transport markers without assigning ϕ_c to a specific spin configuration.

Supplementary Files

This is a list of supplementary files associated with this preprint. Click to download.

- SupplementaryInformationsubmission.docx